Solar Panel Failure Detection by Infrared UAS Digital Photogrammetry: A Case Study

Leonardo Cardinale-Villalobos *‡, Renato Rimolo-Donadio **, Carlos Meza**

*Department of Electronic Engineering, Instituto Tecnológico de Costa Rica, Santa Clara, Alajuela, Costa Rica

**Department of Electronic Engineering, Instituto Tecnológico de Costa Rica, 30101 Cartago, Costa Rica

(lcardinale@tec.ac.cr, rrimolo@tec.ac.cr, cmeza@tec.ac.cr)

‡ Corresponding Author; Leonardo Cardinale Villalobos, Santa Clara, Alajuela, Costa Rica, Tel: +506 2401 3021

lcardinale@itcr.ac.cr

Received: 11.06.2020 Accepted:13.07.2020

Abstract- Infrared thermal photogrammetry is an attractive solution for the diagnosis of photovoltaic systems. Traditional systems often require high-end drones and expensive cameras, but more recently, low-cost thermal sensors on board of small-scale drone platforms suitable for digital photogrammetry have emerged as a promising approach. Nevertheless, studies evaluating its effectiveness can barely be found in the literature.

Unlike many works in the literature that analyze individual images, through digital photogrammetry it is also possible to create orthomosaics of complete installations or high-resolution maps of segments that cannot be visualized and analyzed properly with single images.

In this work, a photogrammetric thermal analysis methodology with a small-scale drone and a thermal camera is presented and a case of study is analyzed. To validate and quantitatively scale the results, functional tests on the panels were performed and temperature measurements with a thermocouple on the panels were carried out. The results from both single images and orthomosaics confirm that it is possible to obtain qualitative and quantitative information to detect failures in solar panel installations with a low-cost thermal sensor on board of small-scale drone platforms. These results may be useful for defining surveillance and maintenance procedures with low-cost equipment in photovoltaic installations, which can help for early detection of failures, operation with higher efficiency and to achieve longer lifetimes of the panels.

Keywords Photovoltaic system, Photogrammetric techniques, Infrared thermal imaging, Unmanned aerial vehicle, Solar panel.

1. Introduction

Steady cost reduction in photovoltaic (PV) solar technology has made it possible to significantly increase the number of installations worldwide. PV installations with hundreds of thousands of PV modules that occupy thousands of hectares are not uncommon [1]. In grid-connected solar installations, PV modules are connected in series, forming strings that are then connected in parallel. In this scenario, a fault in a single cell in a PV module affects all the modules electrically connected to it.

In this context, techniques related to the operation and maintenance of PV modules acquired greater importance. As reported in [2], expert visual inspection and fault analysis in a 3 MW installation take 60 days. Thus, developing techniques that diagnosticate faults efficiently in shorter times becomes a necessity.

Multiple failures can manifest in solar modules, some of them are shading and hot spots [3, 4, 5]. Shading exists when there are cells of a solar panel that are subjected to less solar radiation due to external shadows (see Fig. 1) [6, 7, 8, 9, 10]. Hot spots exist when at least one solar cell in an illuminated module has a considerably smaller short-circuit current than the other cells [11]. All of the above-mentioned faults cause an efficiency decrease [12, 5, 13, 14], i.e., they correspond to sub-optimal operating conditions.

Fig. 1. Example of a solar panel with a partial shadow.

Infrared thermography (IT) is a failure detection technique [15], which is based on the analysis of thermal images of solar panels [16, 17], it allows the identification of temperature gradients or hot spots that can be associated with panel failures [16, 18, 19]. This failure detection technique does not require contact with the element of interest and generates a large amount of qualitative and quantitative information for each image; this allows the estimation of the temperature of each pixel in the thermogram [11]. Fig. 2 shows a fault detected in a solar panel by a thermogram taken with a drone.

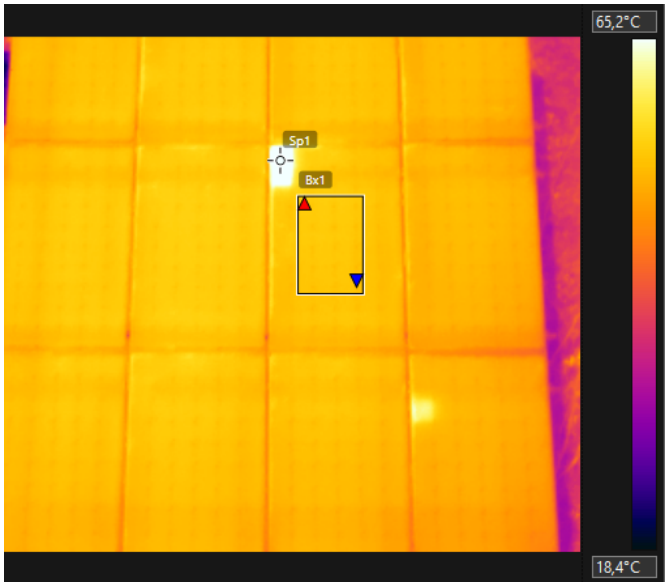

Fig. 2. Solar panel thermogram showing a fault (hot spot), taken with a drone.

The correct application of IT can be complex, especially in the large areas of solar farms with thousands of PV panels. Because the solar panels are oriented upwards and sometimes on roofs, it is often necessary to make the inspections from high points. Unmanned aerial systems (UAS), also known as drones, with onboard thermal cameras, are therefore a useful tool for this task; they enable inspections from the air and through digital photogrammetry techniques it is possible to detect failures in an agile way [11, 20]. Fig. 2 shows an example of a thermogram taken with a drone.

Due to the variety of failures and a large number of solar panels that can be involved in an inspection, the capabilities of the drones and the requirements for IT analysis demand a systematic engineering planning for each mission that include both photogrammetry and individual thermograms [21, 11].

This article demonstrates that it is possible to detect failures in solar panels with low-cost drones and thermal cameras, both through individual image and orthomosaic analysis, applying procedures similar to those available in the literature that had been validated with high-end equipment. This work provides an approach that might contribute making decisions in the maintenance management of photovoltaic systems.

The article is structured as follows: Section 2 discusses briefly previous works and the tools and methods applied, section 3 addresses the configuration of the experiment, and section 4 shows the results with their respective analysis. Section 5 gathers the main conclusions and perspectives for further work.

2. Photovoltaic fault detection and infrared thermal photogrammetry

Two main aspects of fault detection are considered in this work: the presence of hot spots and partial shading. After discussing briefly both cases, the basics for their assessment through UAS imagery and photogrammetry are discussed in this section.

2.1. Thermal imaging characterization of solar panels with hot spots

In a solar panel, multiple failures manifest as hot spots, i.e., small surfaces in a PV cell that exhibit an anomalously high temperature with respect to the neighbouring areas. For example, in [22], the following thermal gradients have been related with faults: a) poor thermal conductivity of the cell's encapsulation material reached 100 °C, b) a micro defect in the cell reached 71.3 °C and c) deformations in resins with a temperature of 136.1 °C. In [11], hot spots were detected due to: cell breaks, false contacts, defective welds, and inactive modules due to bypass diode failures [11].

A hot spot varies in size depending on the type of fault, for example, we can find faults that cover a set of cells (open circuit [11]) or a fraction of the cell (microdefect [22]). Thus, the size of the fault is a parameter that determines the spatial resolution required for the images taken in a drone mission, a parameter known as ground sampling distance (GSD). The temperature variation due to a hot spot is also an indicator of the severity of the fault, where less than 10° is considered within the normal operation tolerance [23, 15]; however, at lower irradiance, the temperature variation of a fault will decrease [24].

2.2. *Characterization of panel thermograms with partial shading*

The region of a solar panel that is found to have lower radiation levels, i.e., it is partially shaded, will experience a higher temperature [21, 25]. This type of hot spot can range from a fraction of a cell (e.g., bird droppings) [11] to multiple cells (e.g., the shadow of an object close to the panel) [21]. According to tests carried out by [26, 27], there may also be cases in which a shadow that covers several cells of the panel, not all or only one, will experience heating. The temperature variation in tests made by [27] with partial shadows was between 10 °C - 20 °C, however, smaller temperature variations were also found.

2.3. *Digital photogrammetry*

Panel faults can be of different sizes and must be detected most of the time over large installations, which imply that a large number of images with good resolution are required. Since from many single images it might be difficult to identify the exact position of the fault, digital photogrammetric techniques can be used for the creation of orthomosaic views of the complete area with georeferencing, thermogram raster and three-dimensional (3D) or 2.5 D profiles of the installation from a set of 2D images.

To apply this technique, images should be taken along a predefined flight route that covers the area under study and provides enough lateral and frontal overlap among images (of at least 60%). The data set is then processed to find coincidence points among images in order to align them, as depicted in Fig. 3. From this step, the matched points are used to project the model in a 3D space in the form of a sparse point cloud. This cloud is refined to create the dense point cloud from which diverse photogrammetric products such as orthomosaics or digital elevation models.

The flow used in this work is based on the well know SIFT and SfM algorithms, implemented in the commercial software tool called Agisoft Metashape, which is the same described in [28, 29].

2.4. *Considerations for implementing photogrammetric surveys*

In our approach, it is assumed that the thermal camera uses an uncooled microbolometer sensor (UMS) that measures infrared radiation and thus estimates the temperature of the object [21]. This means that the camera does not perform a direct measurement of temperature and therefore the acquired images require interpretation.

The measurement should be made at a time with sufficient irradiance to allow the capture of thermal contrasts, with a correct angle and without wind currents that generate convection cooling [21], constant sunlight conditions with a clear sky are also desirable so that solar panels in good conditions have a homogeneous thermal distribution [11]. In [21], it is recommended to have an irradiance between 500 W/m^2 and 700 W/m^2 and to capture the images with an angle between 5° and 60° with respect to the perpendicular of the

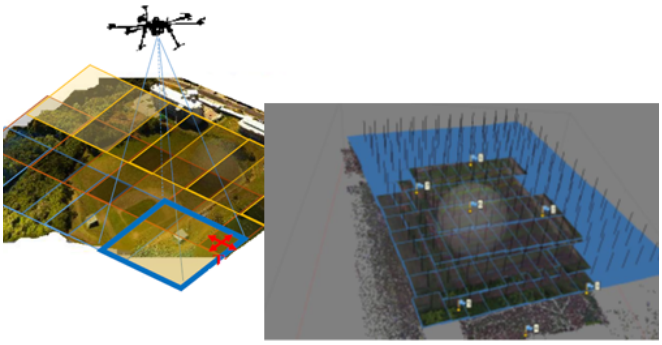

Fig. 3. Illustration of a photogrammetric survey and aligned post-processed images to construct the point clouds.

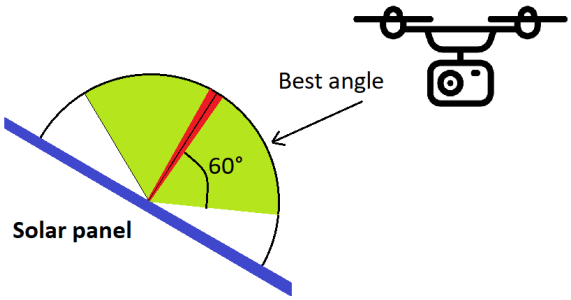

Fig. 4. Recommended orientation of the thermal camera with respect to the panel position.

panel (see Fig. 4). In [15] they indicate that the irradiance should be greater than 700 W/m^2 with an angle between 0° - 30° from the perpendicular direction. Also, the drone can create a partial shadow, so it is recommended to take the measurements in the morning or the afternoon, when the shadow is no projected on the capture footprint [21].

The height is determined from the required spatial resolution or GSD; according to [30], 15 cm/px are required for quick inspections at panel string level, 5.5 cm/px for annual preventive inspections and 3.0 ± 0.5 cm/px for deep inspections, which, according to IEC TS 62446-3, can detect dirt and white spots at cell level [21].

It is recommended that thermal images are captured with georeferenced metadata (GPS coordinates) that facilitates their photogrammetric processing [21]. In the case of using ground control points for precise georeferencing, it is recommended to use aluminum markers, because in the thermogram they are observed in black color due to their low emissivity [21]. This represents an additional cost in material and time, however, in large facilities where the missions will be repeated and compared many times, this cost is justified [21].

According to [31], the camera's emissivity should be set to 0.90 for crystalline cells, and [15] recommends 0.85.

Concerning the flight speed, it should be low to avoid blurry images. In [32], good results were obtained at 1.0 m/s, in comparison to other experiments with higher speeds in the generation of RGB orthophotos. Of course, flight times must

be adjusted accordingly to the autonomy of the drone and area to be covered.

3. Case Study

A DJI Phantom 4 UAS with a FLIR Thermal camera was used to inspect a photovoltaic installation in operation, using the photogrammetric approach described in section 2. This section describes the site, the flight missions, and configuration settings used.

3.1. PV station analyzed.

The Tecnológico de Costa Rica (TEC) has in its campuses in Costa Rica PV installations with about 1,200 panels that are managed by the Laboratory of Electronic Systems for Sustainability (SESLAB); the energy generated is distributed to different facilities in the campuses [33]. For this article, the 19.4 kW PV station located in Santa Clara, San Carlos, was taken as the evaluation site (see Fig. 5), which has the following characteristics:

1) Configuration: 72 panels distributed in 6 strings of 12 panels in series (see Fig. 6), with 3 monocrystalline and 3 polycrystalline strings.

2) Dimensions: The panels are 1650 mm x 992 mm and the strings are 4.95 m x 3.97 m.

3) Geolocation WGS-84: 10.361085, -84.509056.

An RGB picture taken with the drone is shown in Fig. 6.

Fig. 5. Aerial photograph of TEC's photovoltaic station (identified in red) located in San Carlos. Source: Google Maps.

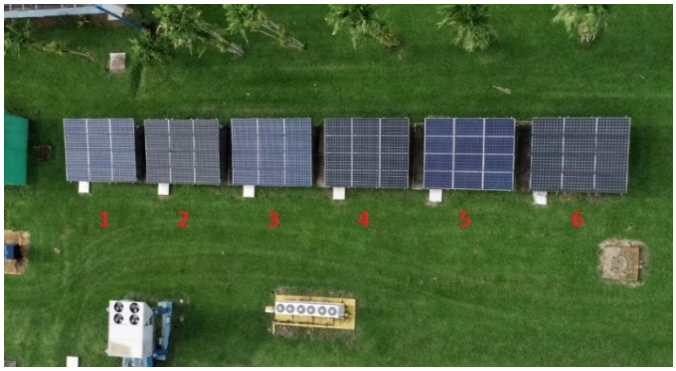

Fig. 6. Aerial photograph of the photovoltaic installation, where each string is identified.

3.2. Description of the UAV and thermal camera.

A commercial Phantom 4 Pro multirotor drone was the UAS platform, with a thermal camera attached. According to the manufacturer, the drone (see Fig. 7) weights 1388 g and a flight time of 30 minutes without the thermographic system.

Fig. 7. Drone with RGB and thermal camera used in this work.

To use the thermal camera with the drone, the following components were included: voltage regulator, 7" monitor (to view the camera image wirelessly), LIPO 3S battery, remote control for the thermal camera gimbal, and the FLIR VUE PRO R camera.

Table 1 shows the specifications of the thermal camera. The camera has a fixed focus set by the manufacturer. The color palette range is automatically adjusted to improve viewing; it cannot be adjusted manually.

Table 1. Characteristics of the FLIR VUE PRO R 336 thermal camera [34, 35].

Parameter	Value
HFOV x VFOV	25° x 19°
Sensor (width x height)	5.764 mm x 4.351 mm
Focal length	13.00 mm
Image width x height	336 x 256
Frequency	9 Hz
Weight	4 oz
Accuracy	+/- 5°C o 5% from reading
Spectral band	7.5 µm -13.5 µm
Size	57.4 mm x 44,45 mm x 44,45 mm
Input voltage	4.8 VDC - 6.0 VDC
Power dissipation (Peak)	2.1 W (3.9 W)
Thermal sensitivity	40 mK
Sensor	Uncooled microbolometer

3.3. Thermal camera setup

The camera was configured with the FLIR UAS 2 application. The configuration was done via Bluetooth, starting to take pictures before take-off and then turning off the Bluetooth to avoid interference with the mission. Table 2 shows the configured parameters.

Table 2. Parameters for image capture and thermographic analysis

Parameter	**Value**
Distance	24 m
Emissivity	0.9
Color palette	Fusion
Humidity	>60 %
Reflected temperature	22 °C
Average Atmospheric Temperature	30 °C
Interval between captures	1 s
File extension	RJPEG for Still Images / Tiff for Orthomosaic

3.4. Orientation used for the thermal camera.

To satisfy the premises indicated in section 2.4, the inclination of the panels α = 9° must be considered. The orientation used with respect to the vertical plane β + α was 30° (β = 21°) (see Fig. 8).

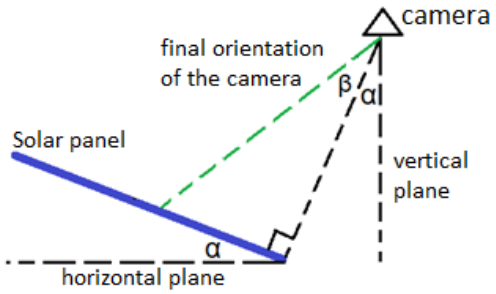

Fig. 8. Diagram of the orientation of the thermal camera relative to the solar panel.

3.5. Flight Plan.

The route of the mission was made manually following the recommendations in section 2.4. The route used is shown in Fig. **9**.

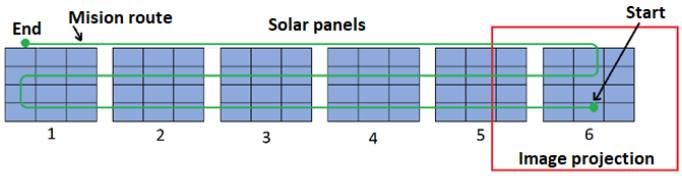

Fig. 9. Route employed in the infrared photogrammetry mission.

With Eq. (1) [36], the height to reach an effective GSD of 3.0 cm/pixel was determined.

$$h = (f_r \cdot Image_{width} \cdot GSD)/(100 \cdot S_W) \quad (1)$$

where f_r is the focal length of the image sensor, $Image_{width}$ is the footprint of the image on the panel and S_w is the size of the sensor. This was adjusted considering 1.3 m (see Fig. 10) of the solar minimum panel height, resulting in a maximum flight height (h) of 24 m from the take-off ground level.

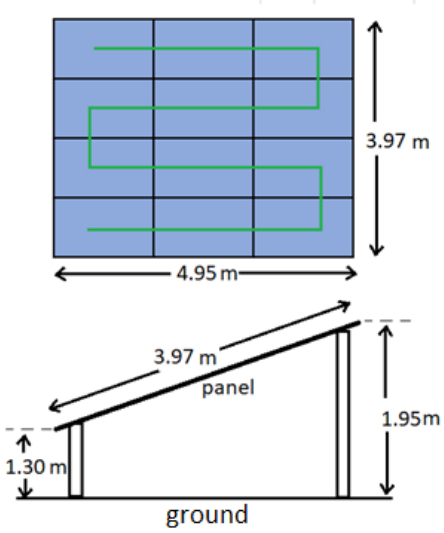

Fig. 10. Top and side view diagram of a solar panel string. The green line represents the way they are electrically interconnected

4. Results and discussion

4.1. Generation of the orthomosaic.

The mission reported here was performed on November 9, 2019, with the following considerations: flight height of 23.7 m, the thermal camera was turned on 60 min before the flight to achieve greater stabilization in the temperature of the camera, and the images began to be taken at 14:48 h local time with 96% battery and ended at 14:57 h with 32% of charge. Additional images were taken and the drone landed at 14:59 h with 20% of battery charge.

The weather was partially cloudy with an irradiance of 523 W/m2, the ambient temperature of the camera was set to 30 °C, and the drone flight speed was less than 1 m/s. Because the mission was manual with low flight speed, the effective overlap was greater than required (90%). Images were taken every second independently of the drone's operation, generating approximately 600 images during the mission. It was found that with a mission of 11 min the battery was consumed to 20% (remaining charge to switch to the "return to home" mode), showing that the autonomy decreases considerably from the 30 min indicated by the manufacturer under normal conditions (without the additional equipment for thermography measurement). For inspections in larger PV stations, multiple missions would be required or an alternative UAS platform with more flexible payload configuration or capacity could be used.

The data processing was done with Agisoft Metashape v1.5.5. Not required photos were manually removed, processing 525 images. A raster transformation was made (see Fig. 11 for the selected palette) and the processes shown in Table 3 were applied. The photogrammetric process allowed the generation of the orthomosaic in Fig. 12.

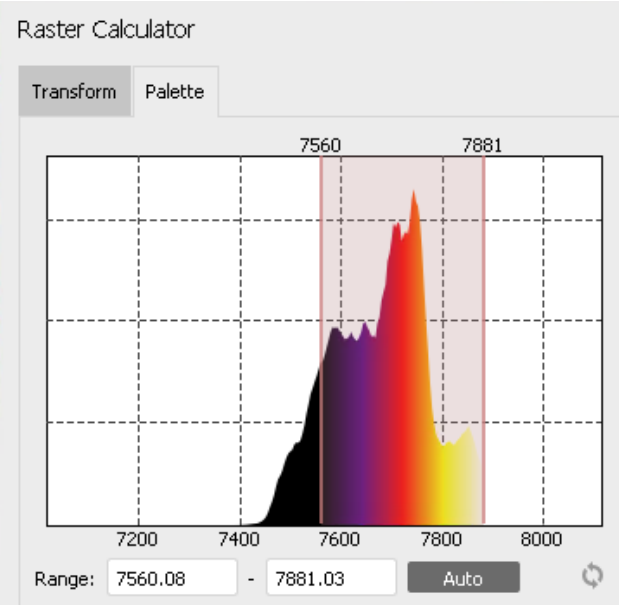

Fig. 11. Color palette assigned for raster processing. Source: image adapted from Agisoft Metashape.

Table 3. Parameters used for the creation of the orthomosaic.

Procedure	Parameters
Align photos	Accuracy: Highest Generic preselection Apply mask to: key points
Build dense cloud	Quality: High Depth filtering: Aggressive Calculate point colors
Build Mesh	Source data: Dense cloud Surface type: Height field (2.5D) Face count: High
Build Texture	Mapping mode: Orthophoto Blending mode: Mosaic Enable hole filling Enable ghosting filter
Build Tiled Model	Source data: Dense Cloud Face count: High Enable ghosting filter
Build Orthomosaic	Type: Planar Projection plane: Top XY Surface: Mesh Blending mode: Mosaic Enable hole filling

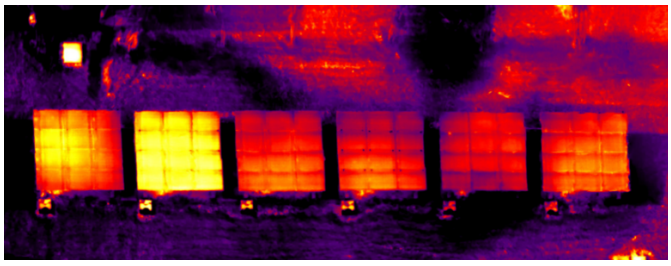

Fig. 12. Orthomosaic generated from the UAS mission.

This process was laborious, requiring masks to be placed on panel strings 1 and 5 due to variations in the tonality of the images by the self-calibration of the camera. A large number of images was used concerning the area covered, however, the processing time for the orthomosaic was 19 minutes with 11 seconds using a server with an Intel Xeon CPU X5675@3.07 GHz, 64 GB of RAM and 4 CUDA GPUs @ 849 MHz with 4096 MB of RAM; the process is relatively fast due to the low resolution of the thermal images in comparison to RGB images that usually require several MB per image.

The orthomosaic generated allowed the apparent temperature of the PV installation to be evaluated from a

qualitative point of view. String 2 was found to have a higher temperature than the others. On strings 5 and 6 a cell was identified as being hotter than its neighboring cells (see Fig. 13). With this, it is shown that the GSD of 3 cm/pixel used is sufficient to visualize thermal information at the cell level, which meets the requirements, mentioned in 2.4, to detect hot spots and partial shadows; however, this will be possible only if the orthomosaic has no distortion at the cell level. Regarding the heating of string 2, it was later found that the associated panels were not in operation due to an undetected failure in the main switch; this proved the possibility of detecting failures at string level.

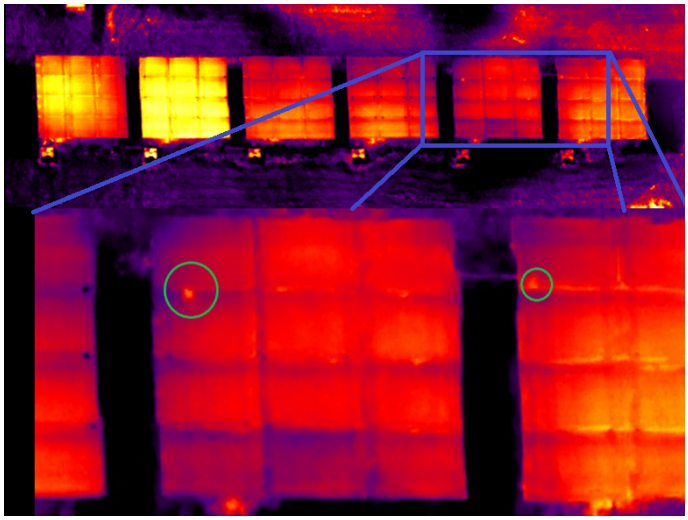

Fig. 13. Identification of cells with higher temperature (indicated in green) in the orthomosaic for string 5 (left) and string 6 (right).

The image processing presented difficulties due to the variation in the tonality of consecutive images due to automatic self-calibration of the camera. Therefore, it is important that the environmental conditions during the mission do not change considerably to avoid obtain different color maps within the images. Although the images could be pre-processed to balance the maps, this issue requires further analysis in future work.

4.2. Individual images.

Since the color map after the photogrammetric process might vary from the actual scale associated with certain temperature levels, after the general inspection it was required to acquire single images at the points where anomalies were detected.

A second mission to collect these additional images was performed on October 29, 2019, using the same protocol as for the orthomosaic mission; about 57 images were taken during the flight, the weather was clear with irradiance between 535 W/m2 - 633 W/m2, the ambient temperature in the camera was set to 30 °C. The image processing was done with the *Flir Tools* application. Forty images were selected, which allowed an analysis of the condition of each string. Two of the processed images are shown in Fig. 14 and Fig. 15.

The results of the individual images are in conformity with those of the orthomosaic since it was also qualitatively identified that strings 5 and 6 have a warmer cell (Fig. 14); the quantitative analysis shows that the cells with higher temperature have a variation of less than 3 °C from those with normal temperature, which is within the expected normal operation range. It was also possible to identify the higher heating of the entire string 2 with respect to the 3 (Fig. 15).

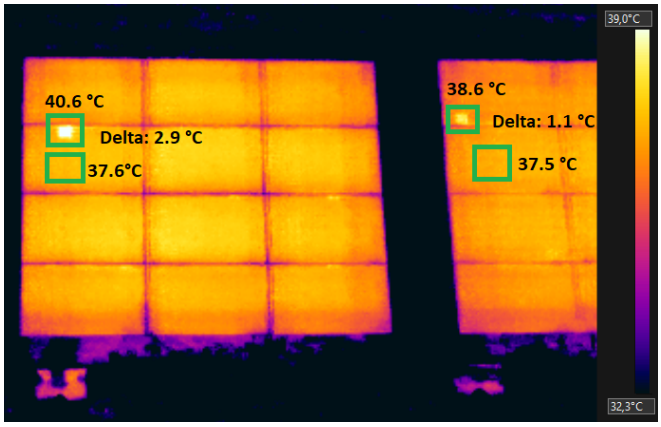

Fig. 14. Thermal image of strings 5 and 6 (from left to right). Two cells are displayed with a higher temperature which after a quantitative analysis indicates a temperature differential of 2.9 °C (left) and 1.1 °C (right).

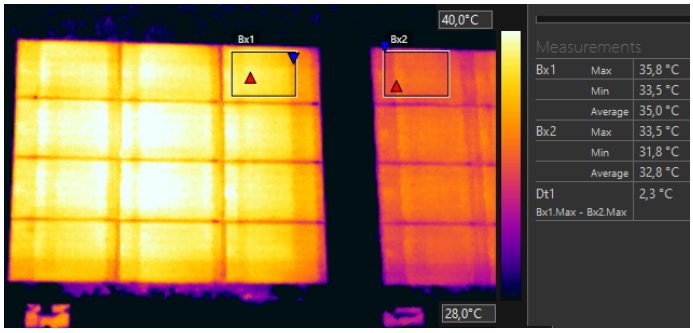

Fig. 15. Thermal image analysis of strings 2 and 3 (from left to right) using Flir Tools software

4.3. Result validation

To validate the thermography estimations, it is possible to perform direct temperature measurements with thermocouples [37, 38], keeping in mind that the aim is not to find the same temperature measurements, since this would require that the measurements be simultaneous to ensure the same environmental conditions, however, the temperature variations must be consistent. To address this, the following procedure was applied between Feb. 27 and March 5, 2020:

a) In strings 5 and 6, measurements were taken with a thermocouple on the back of the hot cell (the cell with the highest temperature in the thermogram) and of another cell with normal temperature. The results are shown in Table 4.

b) An additional thermogram was taken on string 2 (Fig. 16) after correcting the fault detected in the main switch. In this new experiment, a new hot point was found, for which a thermocouple temperature measurement was made to validate the new thermogram (see Table 5).

Table 4. Temperature of the hottest cells identified in strings 5 and 6. On-site irradiance was between 773 W/m^2 and 830 W/m^2.

String	Temperature measured with thermocouple [C°]		
	Hot cell	Reference cell	Difference
5	45	38	7
6	44	41	3

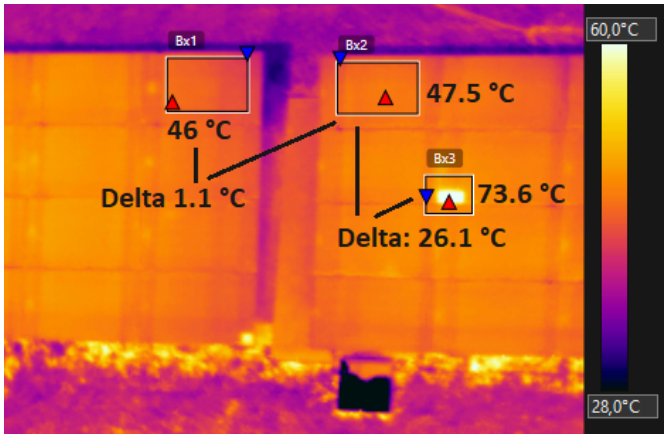

Fig. 16. Analysis of the thermograph of string 1 (left) and string 2 (right) after repairing the false contact in the main switch of string 2.

Table 5. Hot spot measurements of string 2 by thermography and contact measurement.

Measuring mechanism	Temperature (°C)			
	Hot cell	Cold Cell	Difference	Irradiance (W/m^2)
Thermography	73.6	47.5	26.1	932
Contact measurement	65	39	26	886

Table 4 shows that the thermocouple measurement in the hot cells of strings 5 and 6 have a temperature difference of up to 7 °C, in contrast to the thermography where the difference was less than 3 °C (Fig. 14). This is to be expected because the irradiance was higher during thermocouple measurements, which generates more heating in the panels [24]. The results are satisfactory, as they agree with the diagnosis that there is no failure until a difference of 10 °C is present, as mentioned in Section 2.1.

The thermogram of string 2 after correcting the fault in the main switch (Fig. 16) shows a difference of 1.1 °C with respect to a neighbouring string, whereas, with the fault present, it was 2.3 °C (Fig. 15). This indicates that a small temperature increase between strings may indicate a fault, in this case, an open circuit.

The cell with the highest temperature identified in string 2 shows, both with the thermograph and with the thermocouple measurement, a difference in temperature higher than 26 °C (see Table 5), which tells that the quantitative information of the thermograph allows to effectively detect a failure at the cell level.

4.4. Comparison between orthomosaic and individual images

It can be stated from the previous evaluation that the uncalibrated orthomosaic can provide a general overview of the installation, and allows to identify suspicious areas where fails might occur. However, this approach in its current form does not provide precise quantitative information.

In contrast, with individual thermograms, it is possible to obtain quantitative data but without being able to observe the full installation, and this approach can be used as a second pass to inspect suspicious areas observed in the orthomosaic. This means that both, the photogrammetric analysis and thermogram are required and can be viewed as complementary tools to achieve a precise evaluation of a photovoltaic installation.

Although the minimum irradiance conditions indicated in section 2.4 were assured, the greater the irradiance present at the site, the greater the thermal contrast will be when a failure exists [24]; however, this can be a challenge at sites with varying climatic conditions, such as this research site.

5. Conclusions

The results showed that with relatively low-cost equipment it is possible to achieve the necessary autonomy and precision requirements to detect failures, due to hot spots for instance, or inadequate operating conditions such as partial shadows in crystalline silicon photovoltaic installations. The presented approach is very useful in the management of photovoltaic installations, as it may allow extending the life of the system, which also can improve the return of investment and contribute to sustainable development.

Using the applied methodology, individual images allowed detecting failures with reliable quantitative information, although with the difficulty of identifying the string of interest and not achieving a vision of the complete installation. In contrast, the orthomosaic showed a complete picture of the PV installation with a good resolution, enabling qualitative analysis that guided the detection of possible failures at the cell level, identifying the string of interest easily.

Good correlation of thermograms with respect to thermocouples measurements on the panels could be observed. This is a useful resource as a complement to the general uncalibrated orthomosaic obtained through photogrammetry.

The qualitative information of the orthomosaic is useful but can also lead to false positives, as in the case here that two spots on the orthomosaics of strings 5 and 6 were discarded after evaluation of the thermogram. The self-calibration of the thermal camera made it difficult to generate orthomosaic with even color scales, even after giving one hour for stabilization of the temperature in the camera.

The autonomy and stability of the small scale drone used are significantly affected by the inclusion of additional equipment for thermography; therefore, for larger installations, a larger GSD would be necessary or many consecutive missions would be required to cover the entire area. Other UAS platforms with more flexible management of the payload in the same range of price could solve this issue for larger installations.

Future work will address photogrammetric surveying with autonomous flight missions, to reduce the number of images and consequently the mission execution and data processing times. Calibration of the processed orthomosaics, to adjust color maps to actual temperature values, is also a topic for further investigation.

Acknowledgements

This paper is part of a project 5402-1360-4201 “Identificación de Fallas en Sistemas Fotovoltaicos” financed by the Costa Rica Institute of Technology.

References

[1] J. J. Watson and M. D. Hudson, "Regional Scale wind farm and solar farm suitability assessment using GIS-assisted multi-criteria evaluation," *ScienceDirect,* vol. 138, pp. 20-31, 2015.

[2] S. Gallardo-Saavedra, L. Hernández-Callejo and O. Duque-Perez, "Image Resolution Influence in Aerial Thermographic Inspections of Photovoltaic Plants," *IEEE Transactions on Industrial Informatics,* vol. 14, no. 12, pp. 5678-5686, 2018.

[3] W. Chine, A. Mellit, V. Lughi, A. Malek, G. Sulligoi and A. Massi Pavan, "A novel fault diagnosis technique for photovoltaic systems based on artificial neural networks," *Renewable Energy,* vol. 90, pp. 501-512, 2016.

[4] L. D. Murillo-Soto and C. Meza, "Diagnose Algorithm and Fault Characterization for Photovoltaic Arrays: A Simulation Study," in *Springer Lecture Notes in Electrical Engineering (ELECTRIMACS 2019)*, vol. 604, Zamboni W., Petrone G, Springer, Cham, 2020, pp. 567-582.

[5] A. Mellit, G. Tina and S. Kalogirou, "Fault detection and diagnosis methods for photovoltaic systems: A review," *Renewable and Sustainable Energy Reviews,* vol. 91, pp. 1-17, 2018.

[6] T. J. Silverman, L. Mansfield, I. Repins and S. Kurtz, "Damage in Monolithic Thin-Film Photovoltaic Modules Due to Partial Shade," *IEEE Journal of photovoltaics,* vol. 6, no. 5, pp. 1333-1338, 2016.

[7] H. Mekki, A. Mellit and H. Salhi, "Artificial neural network-based modelling and fault detection of partial shaded photovoltaic modules," *Simulation Modelling Practice and Theory,* vol. 67, pp. 1-13, 2016.

[8] S. Choudhury and P. Rout, "AdaptiveFuzzy Logic Based MPPT Controlfor PV System underPartial Shading Condition," *International Journal of Renewable Energy Research,* vol. 5, no. 4, pp. 1252-1263, 2015.

[9] M. Davarifar, A. Rabhi, A. Hajjaji, E. Kamal and Z. Daneshifar, "Partial shading fault diagnosis in PV system with discrete wavelet transform (DWT)," in *2014 International Conference on Renewable Energy Research and Application (ICRERA)*, Milwaukee, WI, USA, 2014.

[10] M.-R. Fazal, Z. Abbas, M. Kamran, I.-u. Haq, M.-N. Ayyaz y M. Mudassar, «Modified Perturb and ObserveMPPT Algorithm for Partial Shading Conditions,» *International Journal of Renewable Energy Research,* vol. 9, nº 2, pp. 721-731, 2019.

[11] J. A. Tsanakas, L. Ha and C. B. , "Faults and infrared thermographic diagnosis in operating c-Si photovoltaic modules: A review of research and future challenges," *Renewable and Sustainable Energy Reviews,* vol. 62, pp. 695-709, 9 2016.

[12] Y. Zhao, "Fault detection, classification and protection in solar photovoltaic arrays," Ph.D. Dissertation, Dept. of Electrical and Computer Engineering, Northeastern University, 2015.

[13] S. Saee, F. Gohar Awa, M. Nasir, M. Mudassa, M. Kamran, A. Nazir and W. Naza, "Analysis of Interconnection Schemes for PV Systems Operating under Shadow Conditions," *International Journal of Renewable Energy Research,* vol. 9, no. 2, pp. 913-922, 2019.

[14] A. Gutierrez, M. Bressan, J. Jimenez and C. Alonso, "Development of real-time supervision HIL emulator of shaded PV systems," in *2017 IEEE 6th International Conference on Renewable Energy Research and Applications (ICRERA)*, San Diego, CA, USA, 2017.

[15] IEA International Energy Agency, «Review of Failures of Photovoltaic Modules,» Performance and Reliability of Photovoltaic Systems, 2014.

[16] S. S. Siva Ramakrishna Madeti, "A comprehensive study on different types of faults and detection techniques," *Solar Energy,* pp. 161-185, 2017.

[17] M. Alsafasfeh, I. Abdel-Qader and B. Bazuin, "Fault Detection in Photovoltaic System Using SLIC and Thermal Images," in *2017 8th International Conference on Information Technology (ICIT)*, IEEE, 2017.

[18] A. Y. Appiah, X. Zhang, B. B. K. Ayawli and F. Kyeremeh, "Review and Performance Evaluation of Photovoltaic Array Fault Detection and Diagnosis Techniques," *International Journal of Photoenergy,* no. 6953530, 2019.

[19] S. Vergura, F. Marino and M. Carpentieri, "Processing infrared image of PV modules for defects classification," in *2015 International Conference on Renewable Energy Research and Applications (ICRERA)*, Palermo, Italy, 2015.

[20] Y. Higuchi and T. Babasaki, "Failure detection of solar panels using thermographic images captured by drone," in *2018 7th International Conference on Renewable Energy Research and Applications (ICRERA)*, Paris, France, 2018.

[21] Y. Zefri, A. ElKettani, I. Sebari and S. Ait Lamallam, "Thermal Infrared and Visual Inspection of Photovoltaic Installations by UAV Photogrammetry—Application Case: Morocco," *drones,* vol. 2, no. 4, p. 41, 23 11 2018.

[22] W. Yadong, . t. Kazutaka, . u. Tsugutomo, K. Keishin and G. Qiang, "Voltage-Based Hot-Spot Detection Method for Photovoltaic String Using a Projector," *energies,* vol. 10, no. 2, p. 230, 2017.

[23] R. Moretón, E. Lorenzo and L. Narvarte, "Experimental observations on hot-spots and derived acceptance/rejection criteria," *Solar Energy,* vol. 118, pp. 28-40, 2015.

[24] M. Cubukcu and A. Akanalci, "Real-time inspection and determination methods of faults on photovoltaic power systems by thermal imaging in Turkey," *Renewable Energy,* vol. 147, pp. 1231-1238, 2020.

[25] T. Yamamoto, D. Wagi and I. Nanno, "New Coupled Model for Prediction of the Temperature Distribution in a PV Cell with a Hot Spot Induced by Partial Shading," in *2018 7th International Conference on Renewable Energy Research and Applications (ICRERA)*, Paris, France, 2018.

[26] A. S. Chaudhary and D. K. Chaturvedi, "Analyzing defects of solar panels under natural atmospheric conditions with thermal image processing," *International Journal of Image, Graphics and Signal Processing,* vol. 10, no. 6, p. 10, 2018.

[27] A. Dolara, G. C. Lazaroiu and E. Ogliari, "Efficiency analysis of PV power plants shaded by MV overhead lines," *International Journal of Energy and Environmental Engineering,* vol. 7, no. 2, pp. 115-123, 2016.

[28] S. Arriola-Valverde, K. Villagra-Mendoza, M. Méndez-Morales, M. Solórzano-Quintana, N. Gómez-Calderón and R. Rimolo-Donadio, "Desarrollo y Validación de una Metodología para la Cuantificación de la Erosión Hídrica a través de Fotogrametría UAS," *Revista Tecnología En Marcha,* vol. 32, no. 5, pp. 43-52, March 2019.

[29] S. Arriola-Valverde, K. Villagra-Mendoza, M. Méndez-Morales, M. Solórzano-Quintana, N. Gómez-Calderón and R. Rimolo-Donadio, "Analysis of Crop Dynamics Through Close-Range UAS Photogrammetry," in *Food CAS, IEEE International Symposium on Circuits and Systems*, Seville, Spain, 2020.

[30] FLIR, "A guide to inspecting solar fields with thermal imaging drones," 16 07 2019. [Online]. Available: https://thermalcapture.com/wp-content/uploads/2019/08/pv-system-inspection-thermal-drones-07-15-19.pdf. [Accessed 11 06 2020].

[31] A. Riverola, A. Mellor, D. A. Alvarez, L. F. Llin, I. Guarracino, C. N. Markides and N. Ekins-Daukes, "Mid-infrared emissivity of crystalline silicon solar cells," *Solar Energy Materials and Solar Cells,* vol. 174, pp. 607-1615, 2018.

[32] G. Y. Jeong, T. N. Nguyen y D. K. Tran, «Applying unmanned aerial vehicle photogrammetry for measuring dimension of structural elements in traditional timber building,» *Measurement,* vol. 153, p. 107386, 2020.

[33] C. Meza, H. Sanchez, F. Monge, J. Morera and A. Mendez, "Estrategia para la implementación de iniciativas sostenibles en ciudades universitarias ejemplificada con el Complejo Solar del TEC de Costa Rica," in *II Ibero-Ameriacan Congress of Smart Cities (ICSC-CITIES2019)*, Soria, Spain, 2019.

[34] Flir, "Flir Vue Pro and Flir Vue Pro R," 2019. [Online]. Available: http://www.flir-vue-pro.com/wp-content/uploads/2016/10/FLIR-VUE-Pro-R-Datasheet-TeAx.pdf. [Accessed 11 06 2020].

[35] Flir.com, "Adjusting Sensitivity & Gain On The FLIR Vue Pro R," Flir, 10 10 2019. [Online]. Available: https://flir.custhelp.com/app/answers/detail/a_id/3134. [Accessed 09 07 2020].

[36] W. Linder, "Introduction," in *Digital Photogrammetry*, 4 ed., Springer-Verlag Berlin Heidelberg, 2016, pp. 10-12.

[37] D. Anthony, D. Sarkar and A. Jain, "Contactless, non-intrusive core temperature measurement of a solid body in steady-state," *International Journal of Heat and Mass Transfer,* vol. 101, pp. 779-788, 2016.

[38] E. Rodriguez, J. Mireles, C. A. Terrazas, D. Espalin, M. A. Perez and R. B. Wicker, "Approximation of absolute surface temperature measurements of powder bed fusion additive manufacturing technology using in situ infrared thermography," *Additive Manufacturing,* vol. 5, pp. 31-39, 2015.